JOURNAL OF GEOPHYSICAL RESEARCH, VOL. 104, NO. B9, PAGES 20,257–20,275, SEPTEMBER 10, 1999

Shallow structure of the Landers fault zone from explosion-generated trapped waves

Yong-Gang Li and Keiiti Aki

Department of Earth Sciences, University of Southern California, Los Angeles

John E. Vidale and Fei Xu

Department of Earth and Space Sciences, University of California, Los Angeles

Abstract. With fault-zone trapped waves generated by near-surface explosions within the fault zone of the 1992 Landers, California, earthquake and recorded by linear seismic arrays deployed along and across the fault, we have delineated the shallow seismic structure near the 30-km-long southern rupture on the Johnson Valley fault. The explosion-excited trapped waves with relatively large amplitude and long-duration wave train after the *S* waves are similar to those generated by aftershocks [*Li et al.*, 1994a, b] but have lower frequencies and travel more slowly. Coda-normalized amplitude spectra of explosion-excited trapped waves show a maximum at ~2 Hz, which decreases rapidly with the station offset from the fault trace on the cross-fault profiles. Normalized amplitudes of trapped waves on the along-fault profile also decreased with distance between the explosion and station, giving an apparent Q of ~18 at 1-2 Hz in the fault zone for the shot near the profile. The dispersion of trapped waves from 0.6 to 2.5 Hz recorded on this along-fault profile implies a shear velocity of ~1.0 km/s for the fault zone and ~1.8 km/s for the wall rock, while the data from the farther shot show an increase in velocity and Q with depth. Measured group velocities and Q values were used as constraints in the numerical modeling of trapped waves on cross-fault and along-fault profiles. Results reveal that the shallow Johnson Valley fault is marked by a zone 250 m wide where the shear velocity is 1 km/s and Q is 20. Calculation of finite difference synthetics for a depth-varying fault structure show that these model parameters apply to the depth of ~1 km, below which the fault zone shear velocity increases to 1.9 km/s and Q increases to 30.

1. Introduction

The fine structure of fault zones is of great interest because the factors that control the initiation, propagation, and termination of rupture are not well understood [*Aki*, 1979; *Scholz*, 1990; *Kanamori*, 1994]. Rupture models have been proposed that involve variations in fluid pressure over the earthquake cycle [*Sibson*, 1977; *Blanpied et al.*, 1992]. Other studies predict that most earthquake energy is stored in areas with less developed fault zones [*Mooney and Ginzburg*, 1986] or with higher velocity rock outside the fault zone [*Eberhart-Phillips and Michael*, 1993; *Nicholson and Lees*, 1992]. Observations suggest that fault zone complexity may segment fault zones [*Lindh and Boore*, 1974; *Aki*, 1984; *Malin et al.*, 1989; *Beck and Christensen*, 1991; *Li et al.*, 1994a] or control the timing of moment release in earthquakes [*Campillo and Archuleta*, 1992; *Harris and Day*, 1993; *Li et al.*, 1994b; *Wald and Heaton*, 1994]. For all these models, knowledge of spatial and temporal variations in fault structure will help predict the behavior of future earthquakes, and such knowledge will help evaluate the models as well.

Structurally, major crustal faults are often marked by zones of lowered velocity with a width of a few hundred meters to a few kilometers [*Thurber*, 1983; *Cormier and Spudich*, 1984; *Mooney and Ginzburg*, 1986]. These low-velocity zones are thought to be caused by an unknown combination of fluid concentrated near faults, clay-rich fault gouge, increased porosity, and dilatant cracks during the earthquake process [*Nur*, 1972; *Sibson*, 1977]. The strength of the low-velocity anomalies might vary over the earthquake cycle [*Vidale et al.*, 1994; *Marone et al.*, 1995; *Massonnet et al.*, 1996; *Li et al.*, 1998a]. The internal structure of major faults is not well understood but may hold the key to understanding how earthquakes come about [*Mooney and Ginzburg*, 1986; *Scholz*, 1990]. Evidence for internal structure of faults has come from inactive exhumed faults [*Chester et al.*, 1993], surface expression of active faults [*e.g., Sieh et al.*, 1993; *Johnson et al.*, 1997], and seismic profiling and tomography [*e.g., Aki and Lee*, 1976; *Louie et al.*, 1986; *Lees and Malin*, 1990; *Michelini and McEvilly*, 1991; *Scott et al.*, 1994; *Thurber et al.*, 1997].

Recently, the fine structure of faults at seismogenic depths has been investigated through fault-zone trapped waves. These waves can be excited by either earthquakes or explosions, as long as the sources are located within the fault zone. Since the trapped waves arise from coherent multiple reflections at the boundaries between the low-velocity fault zone and the high-velocity surrounding rock, their amplitudes and frequencies are strongly dependent on the fault geometry and physical properties [*Li*, 1988; *Li and Leary*, 1990; *Leary et al.*, 1991b; *Li and Vidale*, 1996]. Thus observation and modeling of fault-

Paper number 1999JB900194.
0148-0227/99/1999JB900194$09.00

zone trapped waves can reveal the fine structure and continuity of the fault zone at depth. Fault-zone trapped waves recorded at active fault zones in California and Japan have been used to resolve the fault width of tens to a few hundreds of meters where the shear velocity is reduced by a factor of 25 to 50% and Q is reduced to 20-50 [*e.g., Li et al.*, 1990; *Li and Leary*, 1990; *Leary et al.*, 1991a; *Li et al.*, 1994a, b; *Hough et al.*, 1994; *Malin and Lou*, 1995; *Jongmans and Malin*, 1995; *Ito and Kuwahara*, 1995; *Nishigami et al.*, 1995; *Li et al.*, 1997a, b; *Li et al.*, 1998b]. From the point view of fracture mechanics [*e.g., Rice*, 1980; *Papageorgiou and Aki*, 1983; *Cowie and Scholz*, 1992], we interpret that the low-velocity, low-Q zone is a result of the dynamic rupture in major earthquakes that occurred on these active faults.

However, such analyses have been limited to velocity models that do not vary with depth. For example, we used 3- to 6-Hz trapped waves from aftershocks of the 1992 M7.5 Landers, California, earthquake to delineate the fault. We found to a depth of 10 km that it was marked by a zone with an average width of 180 m, shear velocity of 2 km/s, and Q of 30-50 [*Li et al.*, 1994a]. However, we expect that the increasing pressure with increasing depth will strongly affect the crack density, fluid pressure, and amount of fluids, as well as the rate of healing of damage caused by earthquakes. It may also influence the development of fault gouge [*Scholz*, 1990; *Marone*, 1998a, b]. Because of all these factors, a realistic fault zone is probably not uniform with depth.

This paper describes the shallow structure of the Landers fault using fault-zone trapped waves excited by explosions. The 1992 Landers, California, earthquake broke a fault plane that extended across more than 70 km of the Mojave Desert with a slip of several meters [*Sieh et al.*, 1993; *Cohee and Beroza*, 1994]. The fault breaks the surface over much of its length. The proximity of the earthquake to Los Angeles allowed convenient access for geophysical experiments. These factors motivated us to undertake the most detailed seismic experiments to date in order to measure the internal structure and temporal variation of the Landers fault. We carried out three seismic experiments during 1994-1997 using near-surface explosions along the Johnson Valley fault (the southern Landers rupture segment). P, S, and fault-zone trapped waves were excited by explosions and recorded at linear seismic arrays deployed across and along the fault trace. Repeated surveys have revealed an increase in seismic velocity with time, indicating that the shallow Johnson Valley fault is strengthening after the 1992 earthquake, most likely owing to closure of cracks that were opened by the mainshock [*Li et al.*, 1998a]. The explosion-excited trapped waves are similar to those generated by Landers aftershocks [*Li et al.*, 1994a, b] but have lower frequencies and travel more slowly, suggesting that the fault zone has lower velocities, has lower Q, and probably broadens as it approaches the surface. Similar observations have been obtained from trapped waves generated by microearthquakes and explosions in the San Andreas fault near Parkfield [*Li et al.*, 1997a]. In the present paper, we use explosion-excited trapped waves at 1-2 Hz to document the fine structure of the Johnson Valley fault to a depth of a few kilometers. This is interesting in its own right but is most useful for stripping shallow effects to resolve internal fault zone structure deeper, in the seismogenic zone. A well-imaged fault zone structure is also helpful to localize and understand the fault healing on the shallow Johnson Valley fault.

2. Experiments

In the field experiments we detonated explosions in 30-m-deep shot holes drilled at sites SP2, SP3, SP4, and SP5 (Figure 1 and Table 1), using 500-1000 pounds of chemical emulsions in each hole. Sites SP3, SP4, and SP5 were located within the

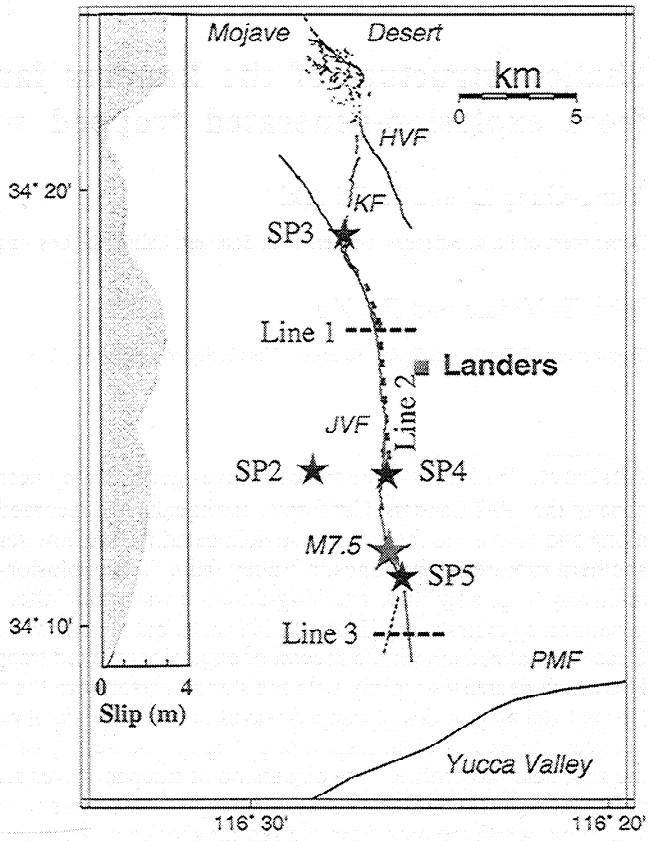

Figure 1. Map of the study region showing locations of three seismic arrays on line 1, line 2, and line 3 (dashed lines) and four explosions (SP2, SP3, SP4, and SP5 (solid stars)) at the fault zone of the 1992 M7.5 Landers, California, earthquake. Only the southern half of the Landers rupture lies within this map, and the dextral surface-fault slip profile is shown (inset) to the left of the map (adapted from *Sieh et al.* [1993]). JVF, Johnson Valley fault; KF, Kickapoo fault; HVF, Homestead Valley fault; PMF, Pinto Mountain fault.

Landers fault zone at distances of 13 and 3 km north and 1.5 km south of the mainshock epicenter, respectively. Site SP2 was located 3 km west of the fault zone. The shot holes were drilled into the hard gray granite rock, uncased at SP2 and SP5 but cased at SP3 and SP4 because of a soft weathering layer at these two sites.

Two linear seismic arrays were deployed on line 1 and line 3 across the Johnson Valley fault (JVF) trace, while one array was deployed on line 2 along the fault trace (Figure 1). The cross-fault lines were about 3 km in length and centered at the fault trace. The location of station ST0 at the center of the cross-fault line is shown in Table 1. The array on line 1 was

Table 1. Locations of Explosion Sites and the Centers of Seismic Arrays at Landers

Site	Latitude N	Longitude W
SP2	34°13'55.43"	116°28'23.75"
SP3	34°19'17.87"	116°27'35.08"
SP4	34°13'45.94"	116°26'11.41"
SP5	34°11'09.37"	116°25'59.57"
ST0 of lines 1, 2	34°16'49.21"	116°26'31.84"
ST0 of line 3	34°09'51.54"	116°25'29.81"

composed of 36 stations. Station spacing was not even; the 16 stations located closest to the fault trace were at 25-m spacing, and the remaining stations were at 50- to 250-m spacing. Line 1 was located 8.7 km north of the mainshock epicenter. The JVF experienced the maximum amount of right-lateral slip of ~3 m and vertical slip of ~1 m near line 1 during the Landers earthquake (Figure 1, inset). The array on line 3 was composed of 21 stations. The 12 stations located closest to the fault trace were at 50-m spacing, and the more distant stations were at 100- to 500-m spacing. Line 3 was located about 4.3 km south of the epicenter. The slip near line 3 is smaller than that near line 1. A minor fault strand crosses the west part of line 3.

The array on line 2 was 8 km in length, composed of 17 stations deployed along the JVF trace with a station spacing of ~500 m. The north end of line 2 was 1.5 km south of SP3. Stations were located on or close to the main fault trace. Several stations were located slightly farther (200-300 m) away from the fault trace because of access problems at those sites. Station ST0 of line 2 was co-located at the station of line 1 on the main fault trace. Fault lines and surface displacements in the survey area were well mapped after the Landers earthquake [*Sieh et al.*, 1993; *Johnson et al.*, 1994].

We used three-channel Refraction Technology (REFTEK) recorders from the PASSCAL Instrument Center of Incorporated Research Institutions for Seismology (IRIS). Sensors (Mark Products 2 Hz L22) were buried at ~0.5 m depth to avoid wind noise. The three components of the sensor at each station were aligned vertical, parallel, and perpendicular to the fault trace. The recorders ran continuously at a rate of 250 samples per second. The data were recorded on an internal 500-M hard disk and then transferred to a Sun desk-top computer in the field. All recorders and shots were synchronized through Global Positioning System (GPS) clocks. The timing errors for recorders and explosions were less than 0.001 s.

3. Results

Figure 2a shows seismograms recorded at the cross-fault array on line 1 for four explosions. Shots SP3, SP4, and SP5 were detonated within the fault zone at distances of about 5, 6, and 10 km from line 1, while SP2 was about 3 km west of the fault zone and 6 km south of line 1. Fault-zone trapped waves with relatively large amplitudes, low frequencies, and long wavetrains following *S* waves were prominent at stations close to the fault trace for explosions detonated within the fault zone. However, trapped waves were not clear at stations farther than 150 m from the fault trace for the same shots. On the other hand, no trapped waves were recorded at any stations on line 1 for explosion SP2 because it was located too far away from the fault zone to excite trapped modes.

In order to analyze trapped waves quantitatively, we calculated the amplitude spectra of seismograms for a 6-s time window (1500 samples for Fourier transformation) starting from the *S* arrivals, using a Hanning window with a 60-ms taper. These spectra were normalized using coda waves to eliminate site and source effects on the spectral amplitudes of trapped waves. This normalization also minimized problems that could arise if the instrument response was not accurately known.

The amplitude spectra of coda waves were calculated in a time window with the same length starting at 30 s after the explosion time. Normalized amplitude spectra on line 1 for three shots detonated within the fault zone showed a maximum at ~2 Hz at stations located close to the fault trace, which decreased rapidly with the distance from the fault trace (Figure 2b). However, no maximum peak at frequencies below 3 Hz was registered at all stations on line 1 for shot SP2, detonated 3 km west of the fault zone, while the amplitudes at frequencies > 3 Hz decreased obviously at stations located east of the fault zone. We interpret the amplitudes at frequencies < 3 Hz to be mainly contributed by fault-zone trapped waves, while amplitudes at frequencies > 3 Hz were due to *P* and *S* waves.

At line 3 across the southern JVF, we also observed prominent trapped waves when both the explosion and stations were located close to the fault trace. For example, Figure 3a illustrates the data recorded at the cross-fault array on line 3 from explosions SP5 and SP2. SP2 and SP5 were located about 7 and 3 km north of line 3. Trapped waves were recorded at stations near the fault trace for SP5, detonated within the fault-zone, but not for SP2, detonated outside the fault zone. Normalized amplitude spectra of seismograms from SP5 showed a maximum at 2-2.5 Hz at stations with the offset less than 150 m from the fault trace, which decayed rapidly at farther stations (Figure 3b). The amplitudes at ~2 Hz were mainly attributed to fault-zone trapped waves generated by the explosion located within the fault zone. In contrast, none of the stations registered maximum amplitudes at 2 Hz for SP2, located far away from the fault zone. We noted that some trapped energy was registered at stations W6-8, probably due to the minor fault strand over there (Figure 1).

We then filtered the seismograms using multiple band-pass filters to study the velocity dispersion of trapped waves. For example, Figure 4 illustrates filtered seismograms on line 1 for SP3 in five frequency bands: 0.8-0.9, 1.1-1.2, 1.4-1.5, 1.7-1.8, and 2.0-2.1 Hz. Trapped waves at lower frequencies traveled faster than those at higher frequencies. The seismic energy at higher frequencies is more concentrated within the fault zone. Because of this dispersion and concentration of fault-zone trapped waves in and near the fault-zone, these waves can be used as a high-precision probe to delineate the fine structure of the fault zone.

The dispersion of trapped waves is shown more clearly on the along-fault profiles on line 2. Figures 5a shows seismograms recorded for SP3, which was located 1.5 km north of line 2. Fault-zone trapped waves are present at all stations in the low-pass (< 2 Hz) filtered seismograms, although they are not clear in the raw data because of strong high-frequency *P* and *S* waves. The separation between the arrivals of *S* waves and trapped waves increases with distance between the explosion and station, as expected for trapped waves traveling along the slower fault zone. We noticed a slight change in the slope of arrival times of trapped waves with respect to the distance, probably due to the variation in velocities along the fault zone. We filtered the seismograms using a four-pole Butterworth filter with a 0.1 Hz frequency band, the center of which moves from 0.65 to 2.45 Hz by steps of 0.1 Hz. For example, Figure 5b illustrates the filtered seismograms in five frequency bands: 0.8-0.9, 1.1-1.2, 1.4-1.5, 1.7-1.8, and 2.0-2.1 Hz. Trapped waves at lower frequencies traveled faster than those at higher frequencies We then computed the envelope of band-pass filtered seismograms using a Hilbert transformation. The peak in the envelope indicates the arrival of energy in the specified frequency band. These plots show the dispersion of trapped waves clearly.

Figure 6 gives the data and results from the along-fault profile for shot SP5, which was located 5 km south of line 2. Again, we observed the dispersion of trapped waves on this profile. Trapped waves at lower frequencies travel faster than those at higher frequencies. However, we also noted that the trapped waves from SP5, which have deeper penetration, travel faster than those from SP3, implying a depth variation in fault zone velocities.

We then measured group velocities of trapped waves from multiple band-pass filtered seismograms in along-fault profiles on line 2 for three shots: SP3, SP4, and SP5. Figure 7 shows measured group velocities versus frequency between 0.6

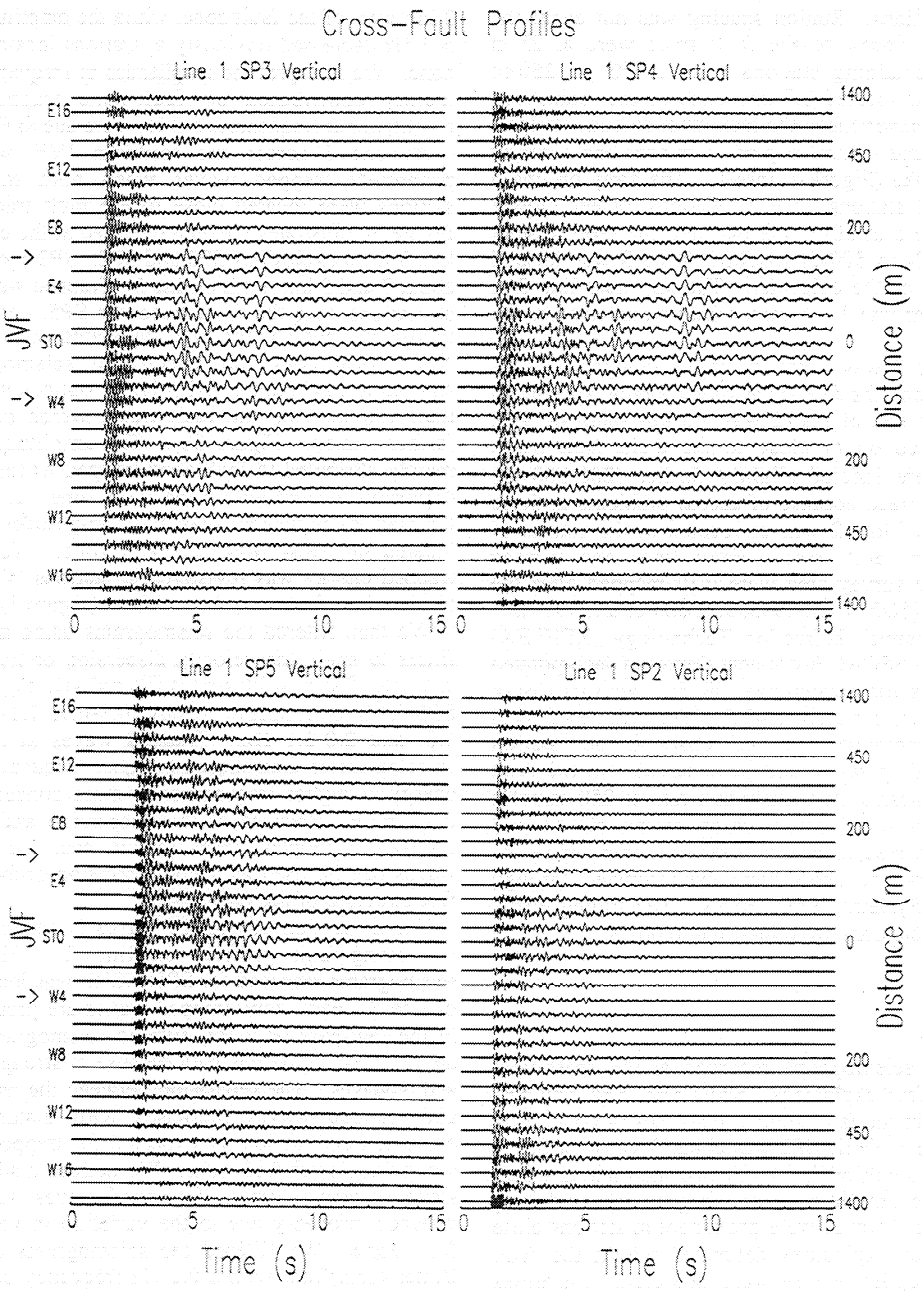

Figure 2a. Vertical component of raw seismograms in cross-fault profiles on line 1 for shots SP3, SP4, and SP5 within the Johnson Valley fault (JVF) and SP2, 3 km away from the fault zone. The station spacing of the array is not even. Station ST0 was located on the mainfault trace of JVF. Seismograms are normalized in each plot. Trapped waves with relatively large amplitude and long period were dominent between 4 and 10 s at stations close to the fault trace for shots detonated within the fault zone. Arrows denote the distance range within which trapped waves are shown clearly. However, trapped waves were not observable at all stations for shot SP2, located far away from the fault zone.

and 2.5 Hz. The group velocities range from ~1.7 km/s at 0.6 Hz to ~1.0 km/s at 2 Hz for shots SP3 and SP4. However, the measured group velocities range from 2.5 km/s at 0.8 Hz to 1.7 km/s at 2 Hz for the farther shot SP5, suggesting an increase in velocities with depth because seismic waves from shot SP5 penetrate deeper in the fault zone than those from SP3 and SP4. These velocity values are used as constraints in our numerical modeling of trapped waves.

In order to evaluate Q value of the fault zone, we calculated coda-normalized amplitude spectra of seismograms recorded on along-fault profiles. Figure 5a (right) illustrates normalized spectra of seismograms on line 2 for SP3, showing a peak at 5 Hz at the station 1.5 km from the shot but a peak at 2 Hz at the station 9.5 km from the shot. The amplitudes at frequencies higher than 3 Hz decay with distance much more rapidly than those at lower frequencies. We have interpreted that the amplitudes at frequencies lower than 3 Hz are mainly attributed to trapped waves, while the amplitudes at frequencies higher than 3 Hz are attributed to body waves. The geometrical spreading is proportional to distance r for body waves but proportional to $1/\sqrt{r}$ for trapped waves, the same as for surface waves [*Aki and Richards*, 1980]. Thus we explain that the

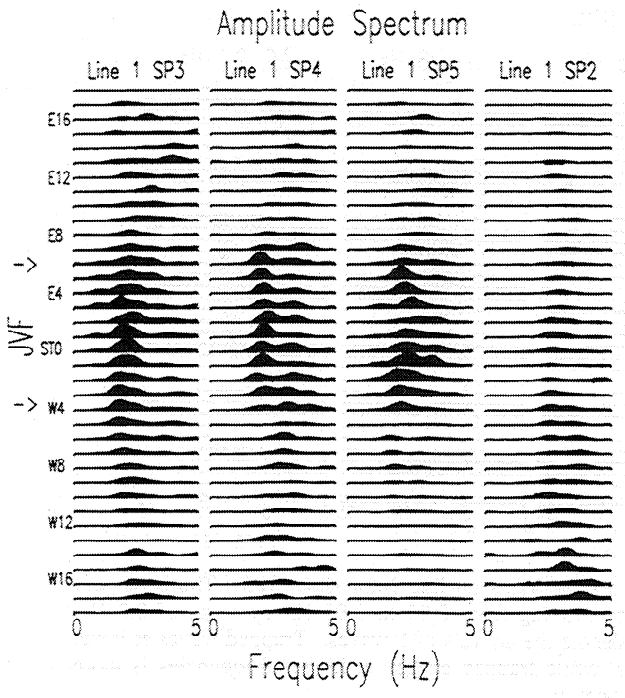

Figure 2b. Coda-normalized amplitude spectra of seismograms shown in Figure 2a. The spectral amplitudes in each panel are plotted using a fixed amplitude scale. The peak amplitudes at ~2 Hz appear at stations close to the fault trace only for SP3, SP4, and SP5 (not for SP2).

rapid decay of amplitudes at frequencies higher than 3 Hz is not only due to the greater attenuation of body waves at higher frequencies but also due to the greater geometrical spreading for body waves than trapped waves.

Figure 8 shows normalized amplitude spectra at 17 stations on line 2 for shot SP3 more clearly. The spectral amplitudes in six frequency bands centered at 1, 2, 3, 4, 5, and 6 Hz with a bandwidth of 0.1 Hz are plotted versus the distance between the stations and SP3. We fit the data using the formula $\ln(A_1/A_i)=\pi f(r_i-r_1)/QV_s$, $i = 1, \cdots, 17$, corresponding to 17 stations, where A_i is the normalized spectral amplitude at the station located at distance r_i from the shot. The amplitude A_i at frequency $f = 1$, 2, and 3 Hz is multiplied by a factor $1/\sqrt{r_i}$ to correct geometrical spreading for trapped waves while the amplitude at $f = 4$, 5, and 6 Hz is multiplied by $1/r_i$ for body waves. V_s is taken on the base of velocities in Figure 7. We obtain the best fit to the data from shot SP3 using Q of 18-22 in the frequency range from 1 to 6 Hz. In the same way, we evaluated Q value from the decay of spectral amplitudes with distance for shot SP5, which was located farther from line 2 than SP3 (Figure 6a, right). We obtained the apparent Q of ~30 at ~2 Hz for SP5, suggesting that the Q value increases with depth. These estimates of fault zone Q values are also used as constraints in the numerical modeling of trapped waves discussed below.

4. Simulations of Fault-Zone Trapped Waves

We first estimate fault zone width, velocity, and Q by synthesis of waves of Love type, using a simple model of an

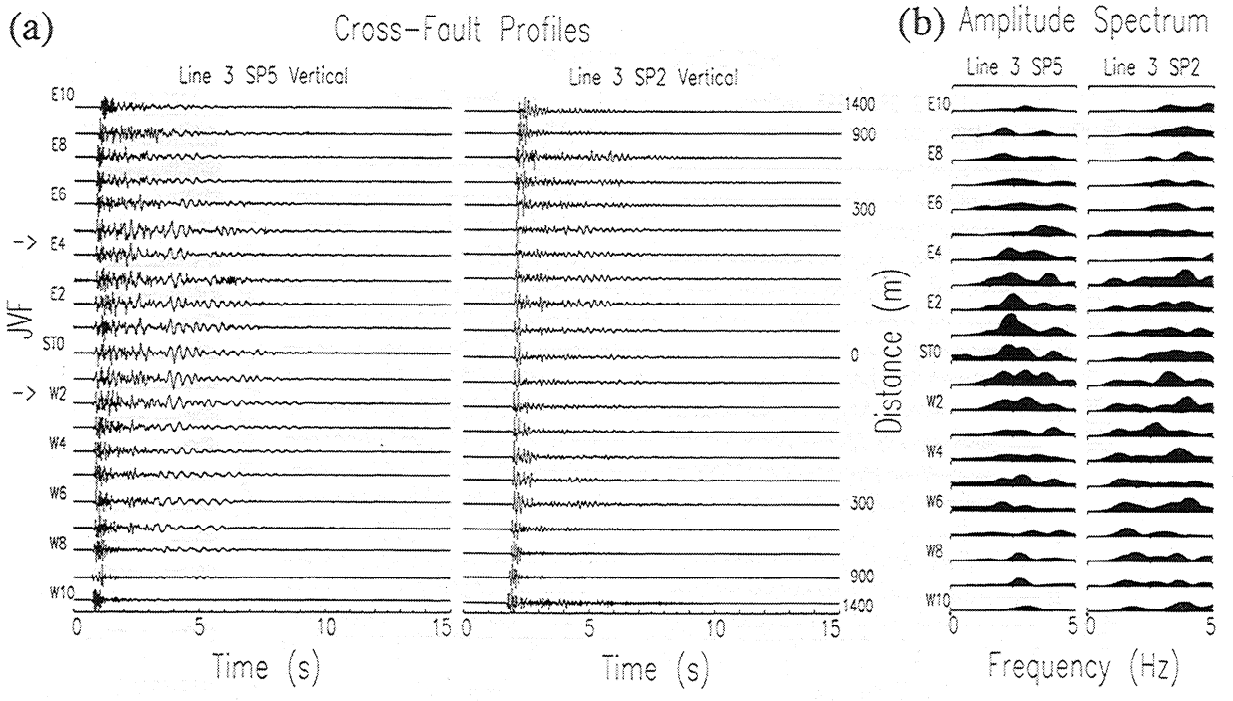

Figure 3. (a) Vertical component of raw seismograms in cross-fault profiles on line 3 for shots SP5 and SP2. Station spacing is not even. Trapped waves were dominent between 2 and 5 s at stations close to the fault trace for SP5 but were not observable at all stations for SP2. Arrows denote the distance range within which trapped waves are shown clearly. (b) Coda-normalized amplitude spectra of seismograms. The spectral amplitudes in each panel are plotted using a fixed amplitude scale. The peak amplitudes at ~2 Hz appear at stations close to the fault trace only for SP5 (not for SP2).

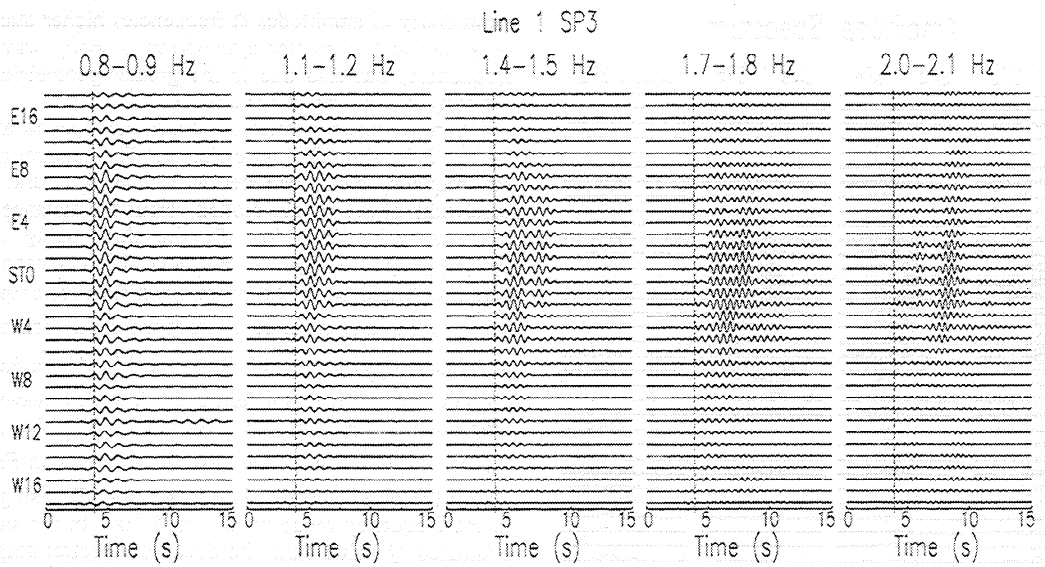

Figure 4. Multiple band-pass filtered vertical component seismograms on line 1 for shots SP3. The band-pass filter has a bandwidth of 0.1 Hz with the central frequency moving from 0.85 to 2.05 Hz by steps of 0.3 Hz. Seismograms are normalized in each plot. The dashed lines denote the arrivals of *S* waves. Trapped waves at lower frequencies traveled faster than those at higher frequencies, while trapped energy at higher frequencies is more concentrated within the fault zone than the lower-frequency energy.

elastic layer with relatively low velocity and Q sandwiched between two elastic half-spaces with relatively high velocity and Q. Next, we compute three-dimensional synthetics for more realistic geometry of the fault zone. In 2-D modeling we use the phase shift method [*Li, 1988; Li and Leary*, 1990] and the formulation for the Love wave part of the Green's function given by *Aki and Richards* [1980] to compute synthetic trapped modes for the first-order fit to observed trapped waves. The speed of 2-D approach allows inversion and sensitivity tests for various model parameters. We have previously used this method at the San Andreas fault near Parkfield and elsewhere [*Li et al.*, 1990, 1994a, 1997a, 1998b].

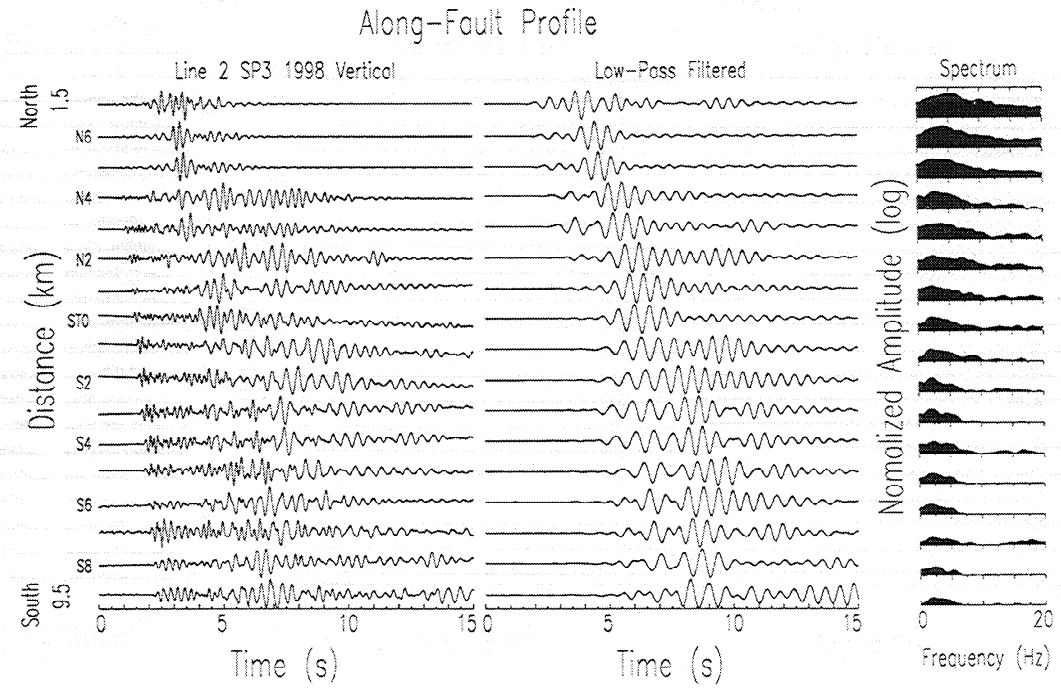

Figure 5a. (left) Vertical component seismograms in the along-fault profile on line 2 for shot SP3. The north end of line 2 was 1.5 km south of SP3. Station spacing is ~500 m. Seismograms are plotted in trace-normalized profile. (middle) Low-pass filtered (< 2 Hz) seismograms. Trapped waves are dominent in the filtered data. The separation between the *S* waves and trapped waves increases with distance. (right) Coda-normalized amplitude spectra of seismograms. Spectral amplitudes are plotted using a logarithmic scale of $10^{0\text{-}4}$, showing a peak at 5 Hz at the station located 1.5 km from SP3 but a peak at 2 Hz at the station 9.5 km from the shot.

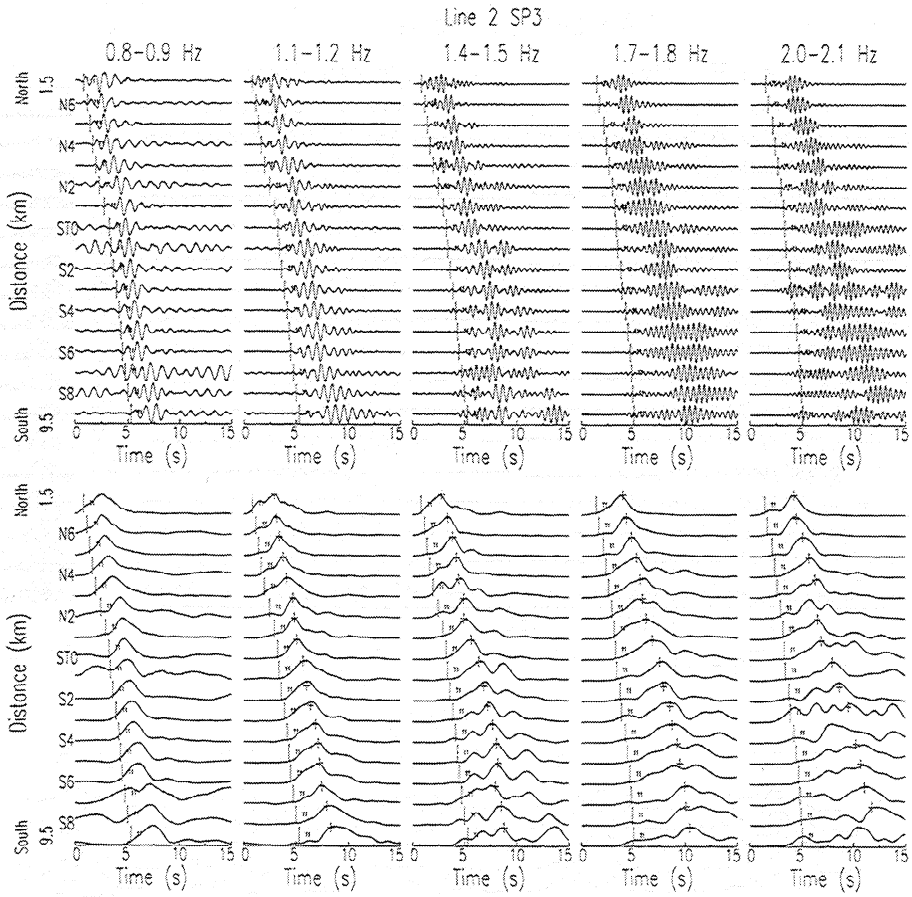

Figure 5b. (top) Band-pass filtered vertical component seismograms on line 2 for shot SP3 in five frequency bands: 0.8-0.9, 1.1-1.2, 1.4-1.5, 1.7-1.8, and 2.0-2.1 Hz. Seismograms are plotted in a trace-normalized profile. Raw seismograms have been deconvoluted to remove the sensor response. The vertical short line on each trace denotes the *S* arrival. Trapped waves at lower frequencies traveled faster than those at higher frequencies. (bottom) Computed envelopes of band-pass filtered seismograms. The peak of envelope marked by a cross indicates the arrival of trapped energy at the specified frequency band.

To find model parameters that best fit the observed trapped waves, we tested various values for the parameters of the waveguide width, velocity and Q, and wall rock velocity, and Q as well as the source and receiver locations. There are trade-offs among these model parameters when we use trapped waves to delineate the structure of a fault zone [*e.g., Li and Leary*, 1990; *Leary et al.*, 1991a; *Li and Vidale*, 1996; *Ben-Zion*, 1998]. However, the trade-offs can be reduced when we have independent estimates of some parameters. For example, in our modeling of trapped waves recorded across the Nojima fault from Kobe aftershocks [*Li et al.*, 1998b], we used the measurements of fault width and velocities in a borehole drilled through the shallow Nojima fault [*Ito*, 1996] as constraints. In the present study at Landers, locations of explosions and seismometers are known. We have measured group velocities and Q values from the dispersion and attenuation of trapped waves along the fault zone. Using these measurements as constraints allowed us to fairly tightly determine the model parameters.

In the modeling procedure we varied model parameters in the ranges shown in Table 2. We obtained the best fit to observations on line 1 and line 2 for shot SP3 using model parameters: waveguide width 260 m, shear velocity 1.0 km/s, and Q of 20; wall rock velocity 1.8 km/s and Q of 35; the source and receivers located within the waveguide, with 80-m offset from the center of the waveguide. Figure 9 shows synthetic dispersion curves, spectral amplitudes, and waveforms of trapped waves using model parameters given above for comparison with the data recorded at the 17 stations on line 2 for shot SP3. The computed dispersion curve matches the measured group velocities quite well. Spectral amplitudes show that trapped waves are prominent at frequencies of 1-2 Hz. Synthetic trapped waves in a true amplitude profile show the decay of amplitudes with distance. We also plot a trace-normalized profile to show waveforms at remote stations more clearly. Trapped waves at lower frequencies travel faster than those at higher frequencies. The separation between the *S* and trapped waves becomes larger with distance. To minimize high-frequency body waves, we filtered both the synthetic and recorded seismograms in a frequency range of 0.7-1.8 Hz. Synthetic waveforms are comparable with observations although the recorded seismograms show more complicated later coda. We then filtered synthetic trapped waves using multiple band-pass filters in five frequency bands: 0.8-0.9, 1.1-1.2, 1.4-1.5, 1.7-1.8, and 2.0-2.1 Hz. The dispersion of synthetic trapped waves agrees well with observations in Figure 5b, showing that our 2-D model explains the data.

We further generated synthetic trapped waves in the cross-fault profile (Figure 10) using the model parameters given above for comparison with seismograms recorded on line 1 for shot SP3. Normalized spectral amplitudes of both synthetic and observed seismograms show a maximum peak at 1-2 Hz at stations located within the fault zone, which decreases rapidly

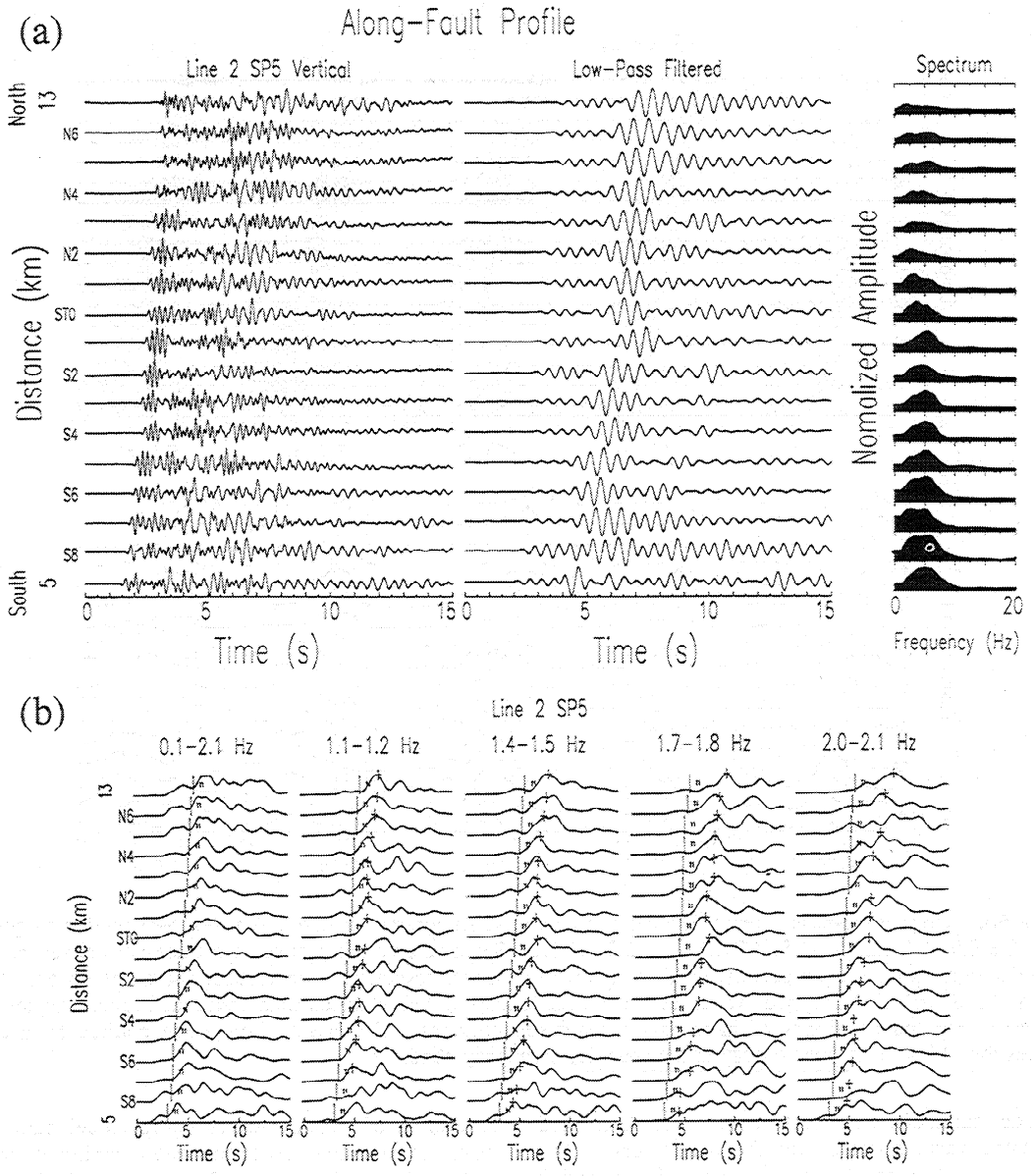

Figure 6. (a) On the left are shown vertical component seismograms in the along-fault profile on line 2 for shot SP5, which was located 5 km south of line 2. Station spacing is ~500 m. In the middle are shown low-pass filtered (< 2 Hz) seismograms. Trapped waves are dominent in the filtered data. The separation between the *S* waves and trapped waves increases with distance. On the right are shown coda-normalized amplitude spectra of seismograms. The spectral amplitudes are plotted using a fixed linear scale for all stations. Other notations are the same as in Figure 5a. (b) Computed envelopes of multiple band-pass filtered seismograms on line 2 for shot SP5. The peak of envelope marked by a cross indicates the arrival of trapped energy at the specified frequency band. Trapped waves at lower frequencies traveled faster than those at higher frequencies. Other notations are the same as in Figure 5b.

with the increasing station offset from the fault. Observed spectral amplitudes at frequencies >3 Hz are larger than synthetic amplitudes because of the high-frequency *P* and *S* waves in the data. On the other hand, observed amplitudes at frequencies <1 Hz are smaller than synthetics, although we have moved the cutoff frequency of the sensor response to 0.6 Hz by deconvolution on recorded seismograms. To minimize effects of body waves and sensor response, both the synthetic and recorded seismograms have been band-pass (0.7-1.8 Hz) filtered for a comparison. We obtain a good agreement between the observed and synthetic waveforms with the cross-correlation coefficient higher than 0.8, showing again that our modeling matches the data.

The examples given below show that the amplitude and dispersion of trapped waves are sensitive to the change of model parameters. Figure 11 illustrates synthetics in the along-fault and cross-fault profiles using different waveguide widths, velocities, *Q* values, and source offsets from the model parameters used for the best fit to the data as shown in Figures 9 and 10. The narrower (150-m-wide) waveguide produces trapped waves at higher frequencies. The smaller velocity contrast between the waveguide (V_S = 1.3 km/s) and wall rock (V_S = 1.8 km/s) produces shorter wavetrains. The higher *Q* (100) waveguide produces larger amplitudes of trapped waves at higher frequencies. When the source is located 250 m away from the waveguide, it generates only weak trapped waves at

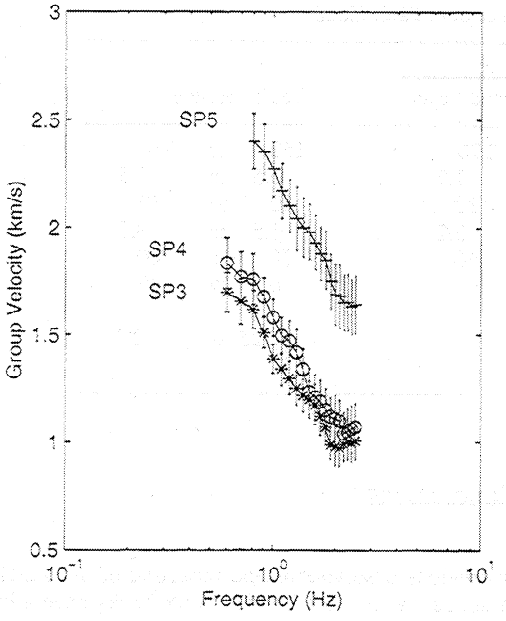

Figure 7. Group velocities of trapped waves measured from multiple band-pass filtered seismograms in cross-fault profiles on line 2 for shots SP3 (stars), SP4 (circles), and SP4 (crosses). Each point denotes the mean value of measurements at the specified frequency for three-component data recorded at 17 stations on line 2. The standard deviation (denoted by the error bar at each point) is smaller than 0.2 km/s.

frequencies <1 Hz. In the trial-and-error modeling we found that when the waveguide width varies by 20 m, or S velocity varies by 0.2 km/s, or Q value varies by 10, the changes in amplitude and dispersion of trapped waves noticeably degrade the fit to the data.

5. Three-Dimensional Finite Difference Simulations

However, the synthetic trapped waves in the two-dimensional (2-D) profiles may be somewhat different from three-dimensional (3-D) sections. To study the differences between 3-D modeling and 2-D modeling, we used more realistic 3-D finite difference simulations for comparison with the 2-D synthetics described above. We used the 3-D finite difference computer code [Graves, 1996]; it is second order in time and fourth order in space. It propagates the complete wavefield through elastic media with a free-surface boundary and spatially variable anelastic damping (an approximate Q). The source can be double couple or an explosion. The first-order elastodynamic equations of motion are solved using a staggered-grid finite difference algorithm. This numerical approach, with a memory optimization procedure, allows large-scale 3-D finite difference problems to be computed on a conventional, single-processor, desk-top workstation.

Figure 12 shows 3-D simulations of seismograms in the along-fault profile on line 2 and the cross-fault profile on line 1 for shot SP3. The calculation uses a 200(x)-by-500(y)-by-200(z) element grid, where the x and y axes are perpendicular and parallel to the fault trace and the z axis is in depth, to simulate a volume that includes the fault zone, explosion, and seismic array. The grid spacing is 25 m. The medium velocity is 3.3 km/s for P waves and 1.8 km/s for S waves, and Q value is 35. A 250-m-wide uniform fault-zone waveguide is sandwiched between two quarter-spaces and placed along the middle of the grid, far enough from the edges of the model that side reflections do not appear in the seismograms. The P and S velocities within the fault zone are 1.8 and 1.0 km/s,

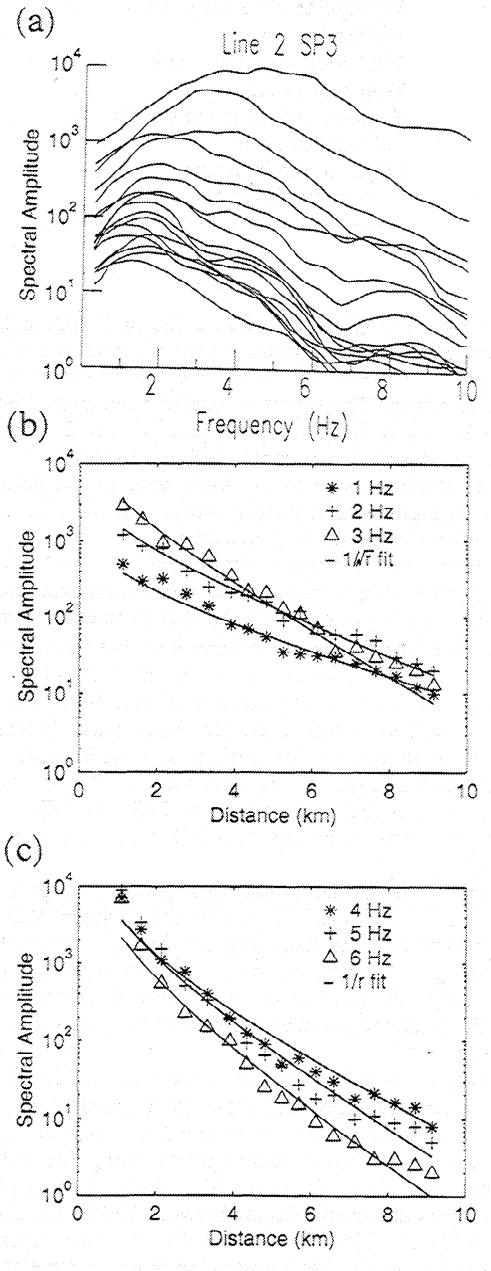

Figure 8. (a) Normalized amplitude spectra of seismograms recorded at 17 stations on line 2 for shot SP3. Each curve comes from three-component data. The amplitudes decay with the distance between the stations and shot. (b) Normalized spectral amplitudes at 1, 2, and 3 Hz versus distance r. Distances of 17 stations from SP3 increase from 1.5 km to 9.5 km with station spacing of 0.5 km. Amplitudes at specific frequencies are taken from Figure 8a. The lines fit amplitudes using Q of 18 and are multiplied by a factor of $1/\sqrt{r}$ for the correction of geometrical spreading for trapped waves. (c) Normalized spectral amplitudes at 4, 5, and 6 Hz versus distance r. The lines fit amplitudes using Q of 22 and are multiplied by $1/r$ for the correction of geometrical spreading for body waves.

Table 2. Waveguide Model Parameters on the Shallow Landers Fault Zone

Model Parameters	Best Fit		Tested Range
	Upper Layer	Second Layer	
Waveguide width, m	250	200	150 to 350
Waveguide S velocity, km/s	1.0	1.9	0.5 to 2.5
Waveguide Q value	20	30	10 to 30
Wall rock velocity, km/s	1.8	3.2	1.5 to 3.5
Wall rock Q value	35	60	20 to 100
Source offset from the middle of waveguide, m	50		0 to 200
Depth of the interface in the two-layer model, km	1.0		0.25 to 2.0

respectively. The Q value is 20 for the fault zone and 35 for the surrounding rock. A point source is embedded within the fault zone at a depth of 50 m and 50 m offset from the waveguide center. The source is located 5 km away from line 1 and 1.5 km away from the north end of line 2. Fault-zone trapped waves with large amplitudes and dispersive waveforms appear at stations close to the fault zone in the across-fault profile. The along-fault profile shows that the time delay of trapped waves increases with distance.

We plot the vertical component of 3-D synthetic seismograms in true-amplitude and trace-normalized profiles in Figure 13 for comparison with the 2-D synthetics (Figures 9d and 9e). We also filtered seismograms in five frequency bands: 0.8-0.9, 1.1-1.2, 1.4-1.5, 1.7-1.8, and 2.0-2.1 Hz for comparison with the 2-D synthetics (Figure 9g). We derived group velocities from multiple band-pass filtered 3-D synthetic seismograms for comparison with those derived from the 2-D synthetics and observations (Figure 14). We obtain a good agreement among the 2-D and 3-D synthetics and observations, showing our 2-D modeling approach is applicable.

However, the model parameters given in Figure 9a are appropriate for the shallow part of the Johnson Valley fault because seismic waves from SP3 can penetrate only a shallow depth owing to the limit to the distance between the shot and seismic array. In section 3 we showed the data from the farther shot SP5, which indicated an increase in velocities and Q value with depth.

To study a more realistic fault zone with the depth-variable structure, we tested how deep these model parameters in Figure 9a can be applied. Here we assumed a two-layer fault zone structure and computed seismograms using the 3-D finite difference code for a suite of models with the interface between the two layers at variable depths between 250 m and 2 km with a step of 250 m. Model parameters for the upper layer are the same as in Figure 9a. We adjusted the model parameters for the second layer in the range shown in Table 2. The measured group velocities and Q value from the along-fault profile for SP5 are used as constraints in modeling. We obtained the best fit of synthetics to observations using the model parameters for the second layer: The shear velocity is 1.9 km/s in the fault zone and 3.2 km/s outside the fault zone; Q is 30 in the fault zone and 60 outside the fault zone; the fault zone width is 200 m; the interface between the two layers is at 1 km. For example, Figure 15a shows vertical component synthetic seismograms in the cross-fault profiles on line 1 for three shots (SP3, SP4, and SP5) using the model parameters for the best fit to the two-layer fault zone structure given in Table 2. The synthetic waveforms agree quite well with the recorded seismograms in the frequency range of 0.7-1.8 Hz (Figure 15b).

6. Conclusions

Our previous observations and modeling of 3- to 6-Hz fault-zone trapped waves from Landers aftershocks have allowed us to evaluate the internal structure and continuity of the rupture zone at seismogenic depth [*Li et al.*, 1994a, b]. However, the results described only the average physical properties of the Landers fault-zone because we assumed a uniform fault structure in 2-D modeling.

In this paper, we showed fault-zone trapped waves generated by near-surface explosions detonated within the Landers fault-zone and recorded at the dense seismic arrays deployed across and along the fault. We used these trapped waves to delineate the Landers fault with high resolution although these waves sampled the shallow part of the fault zone because of the relatively short distance between the shots and arrays. The explosion-excited trapped waves are similar to those generated by aftershocks but have lower frequency (~2 Hz) and travel more slowly, suggesting that the fault zone has lower velocities and lower Q, and probably broadens as it approaches the surface. Similar but less robust observations were obtained in our previous study of the San Andreas fault near Parkfield using trapped waves from earthquakes and explosions [*Li et al.*, 1997a].

We measured group velocities of explosion-excited trapped waves from multiple band-pass filtered seismograms in along-fault profiles at Landers. The measurements show dispersion of trapped waves clearly, ranging from ~1.7 km/s at 0.6 Hz to ~1.0 km/s at 2 Hz for shots at short distances to the seismic array. However, the group velocities measured for the farther shot range from 2.5 km/s at 0.8 Hz to 1.7 km/s at 2 Hz, suggesting an increase in velocity with depth because trapped waves from the farther shot penetrated the deeper in the fault zone.

We measured the Q value of the Landers fault zone from the decay of coda-normalized spectral amplitudes of trapped waves with distance along the fault. The fault zone Q is ~18 for the shallow fault zone and increases with depth too. The measured group velocities and Q values have used as constraints in our numerical modeling of trapped waves. They allowed us to fairly tightly determine the model parameters and reduce trade-offs among model parameters.

In the modeling procedure we first used a 2-D computer code for a uniform fault zone structure. The speed of 2-D approach allows sensitivity tests for various model parameters. We then computed synthetics using a 3-D finite difference code for more realistic geometry of the fault zone and explosion source at Landers. Computation of 3-D synthetics for a two-layer fault model confirms that our 2-D model explains the data correctly in the first-order sense. We obtained the best fit to the data

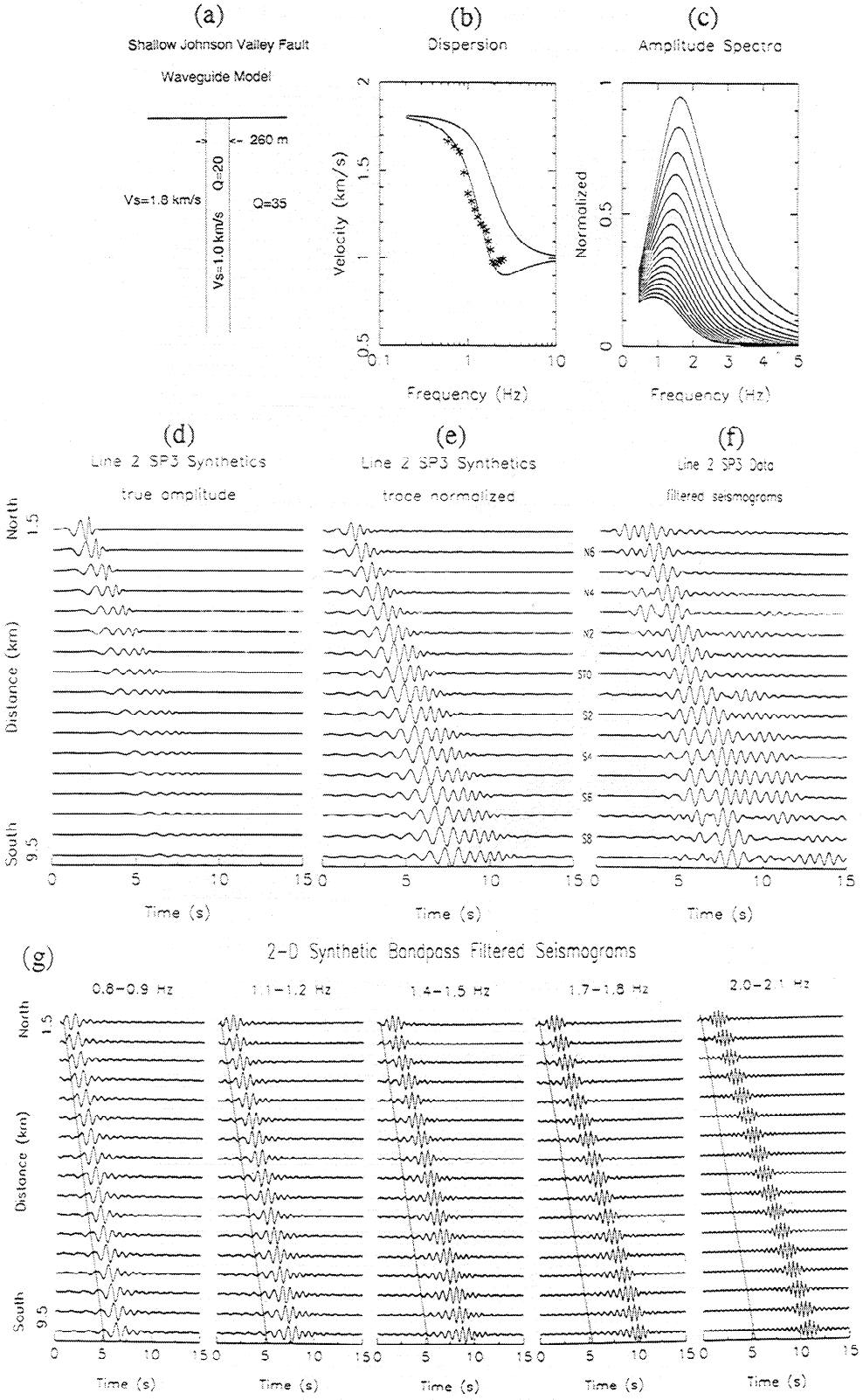

Figure 9. (a) The two-dimensional planar waveguide model of the shallow Johnson Valley fault. Model parameters shown are used to generate synthetic trapped waves best fit to observations on line 2 for SP3. (b) Computed dispersion curves for trapped waves using model parameters given in Figure 9a. Stars are measured group velocities. (c) Computed amplitude spectra at 17 stations on line 2. (d) Synthetic trapped waves in response to a unit source located within the fault zone. Waveforms are plotted using a fixed amplitude scale for all traces. (e) Synthetic trapped waves plotted in a trace-normalized profile. (f) Vertical component seismograms recorded on line 2 for shot SP3. Seismograms in Figures 9e and 9f are filtered in a frequency range of 0.7-1.8 Hz. (g) Band-pass filtered synthetic trapped waves on line 2 for SP3 in five frequency bands for comparison with observations shown in Figure 5b. Solid lines denote synthetic *S* arrivals.

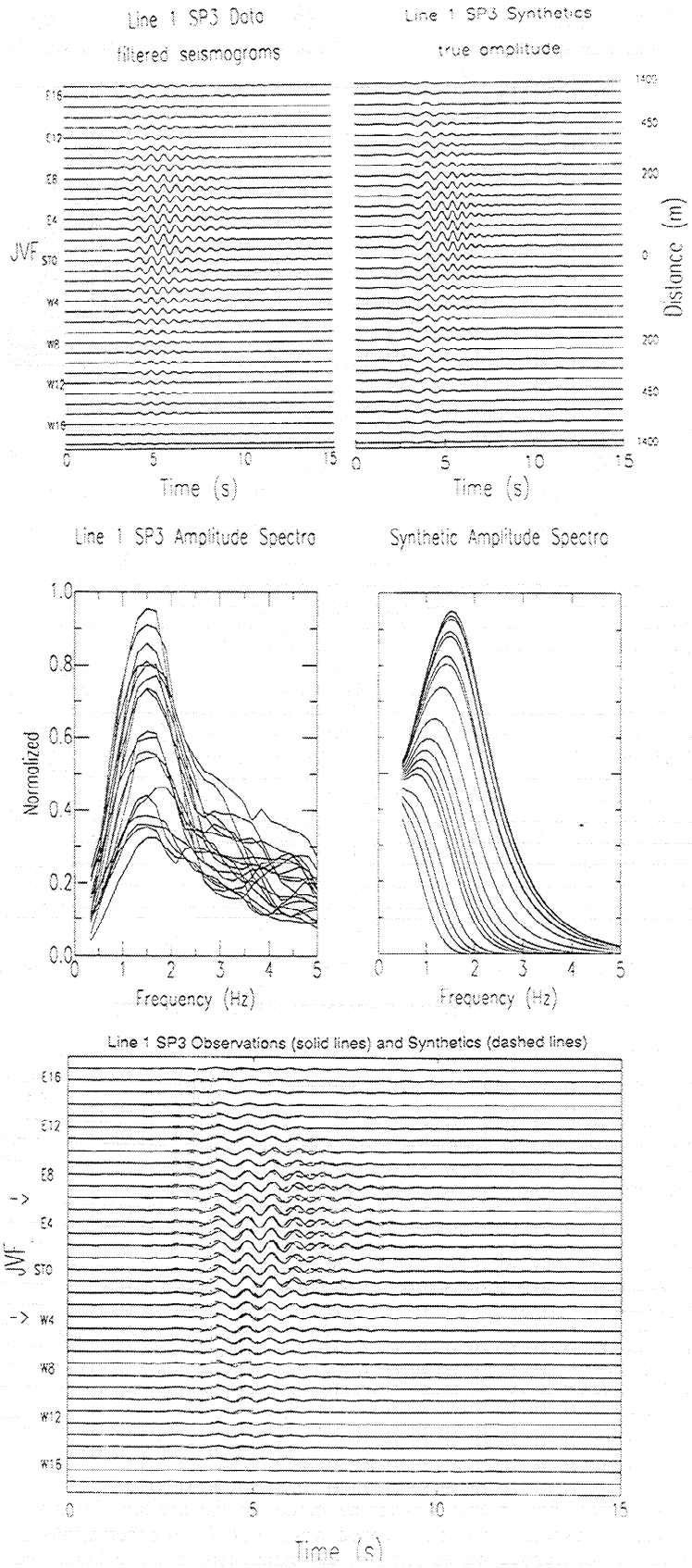

Figure 10. (top) Two-dimensional synthetic seismograms using the model parameters given in Figure 9a and recorded seismograms in cross-fault profiles on line 1 for shot SP3. Seismograms are filtered in a frequency range of 0.7-1.8 Hz and plotted using a fixed amplitude scale for all traces. Station spacings for synthetics are the same as in the field. (middle) Amplitude spectra of synthetic and observed seismograms. (bottom) Synthetic trapped waves (dashed lines) are compared with observed seismograms (solid lines).

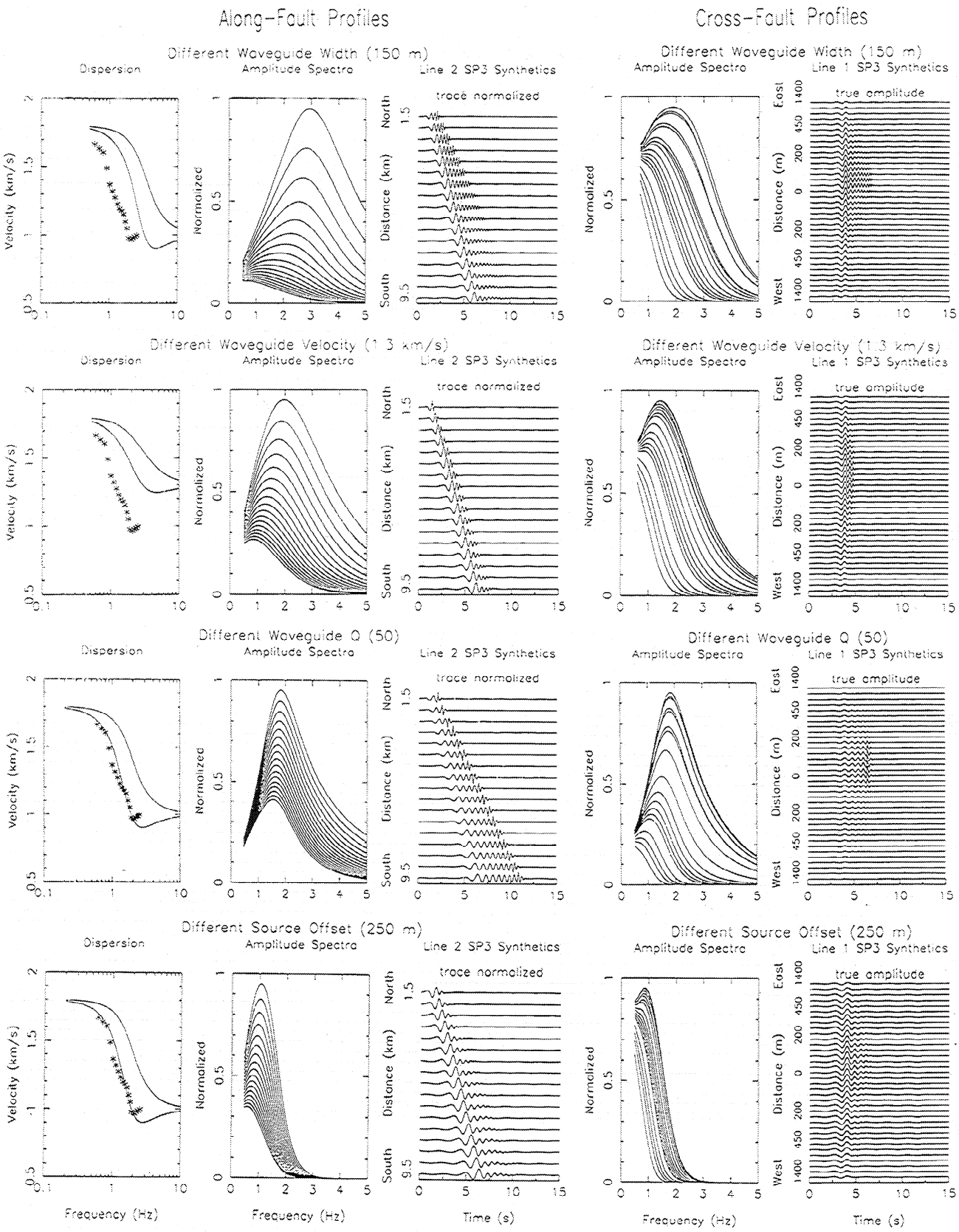

Figure 11. Synthetic dispersion curves, amplitude spectra, and waveforms of trapped waves in along-fault profiles on line 2 and cross-fault profiles on line 1 for shot SP3 using different waveguide width, velocity, Q value, and source offset from model parameters given in Figure 9a. The receiver spacing on line 2 is 500 m. Locations of receivers on line 1 are the same as in the field.

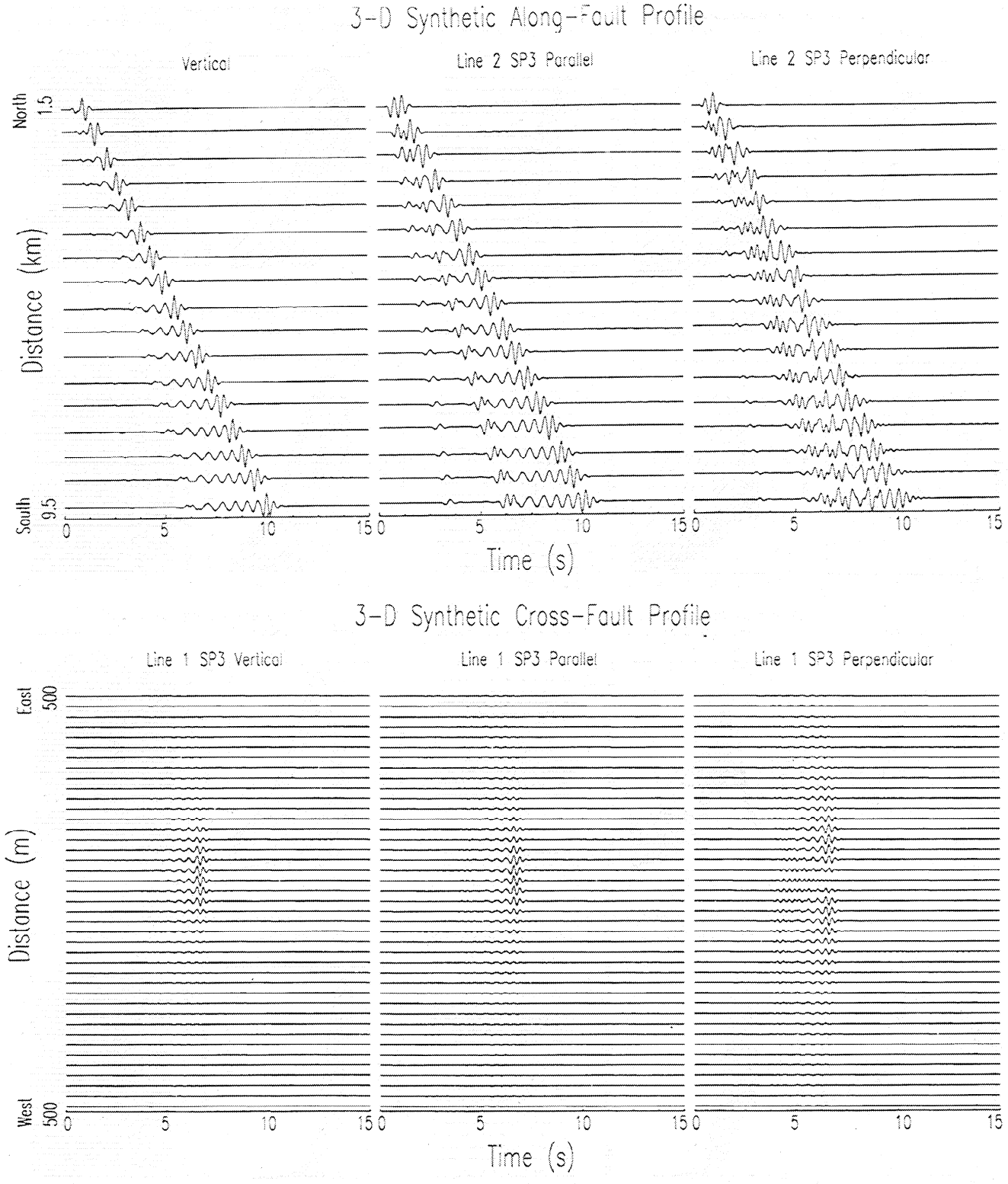

Figure 12. Three-dimensional finite-difference synthetic seismograms in the along-fault profile on line 2 and in the cross-fault profile on line 1 for explosion SP3 using a model with a uniform waveguide. Model parameters are described in the text. Seismograms on line 2 are plotted in a trace-normalized profile with the station spacing of 500 m. Seismograms on line 1 are plotted in true amplitude with the station spacing of 25 m. The waveguide is placed in the middle of the cross-fault profile.

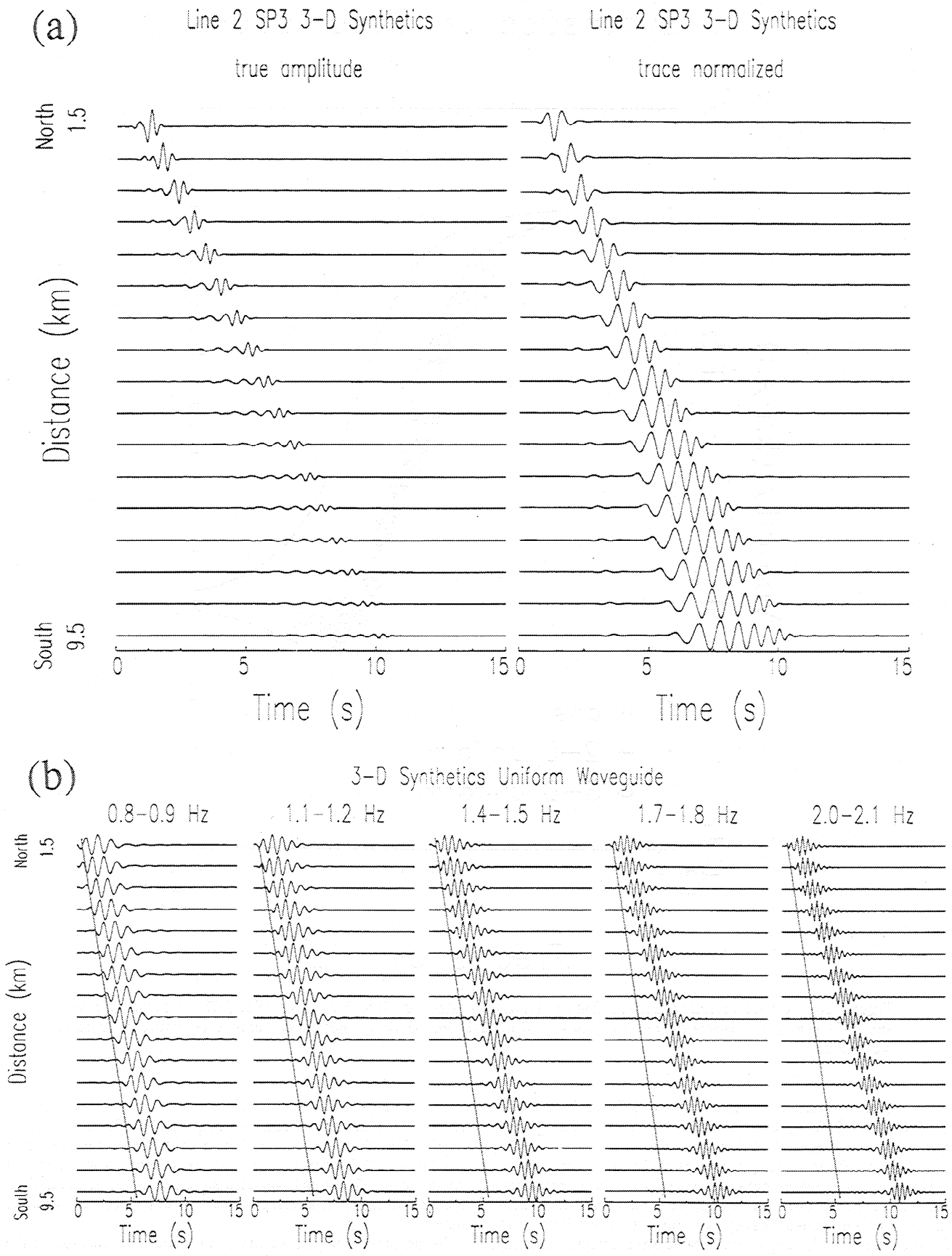

Figure 13. (a) Vertical component 3-D synthetic seismograms on line 2 for SP3 plotted in true-amplitude and trace-normalized profiles for comparison with 2-D synthetics shown in Figure 9d and 9e. Seismograms in the trace-normalized profile have been filtered in a frequency range of 0.7-1.8 Hz. (b) Multiple band-pass filtered 3-D synthetic seismograms for comparison with 2-D synthetics shown in Figure 9g.

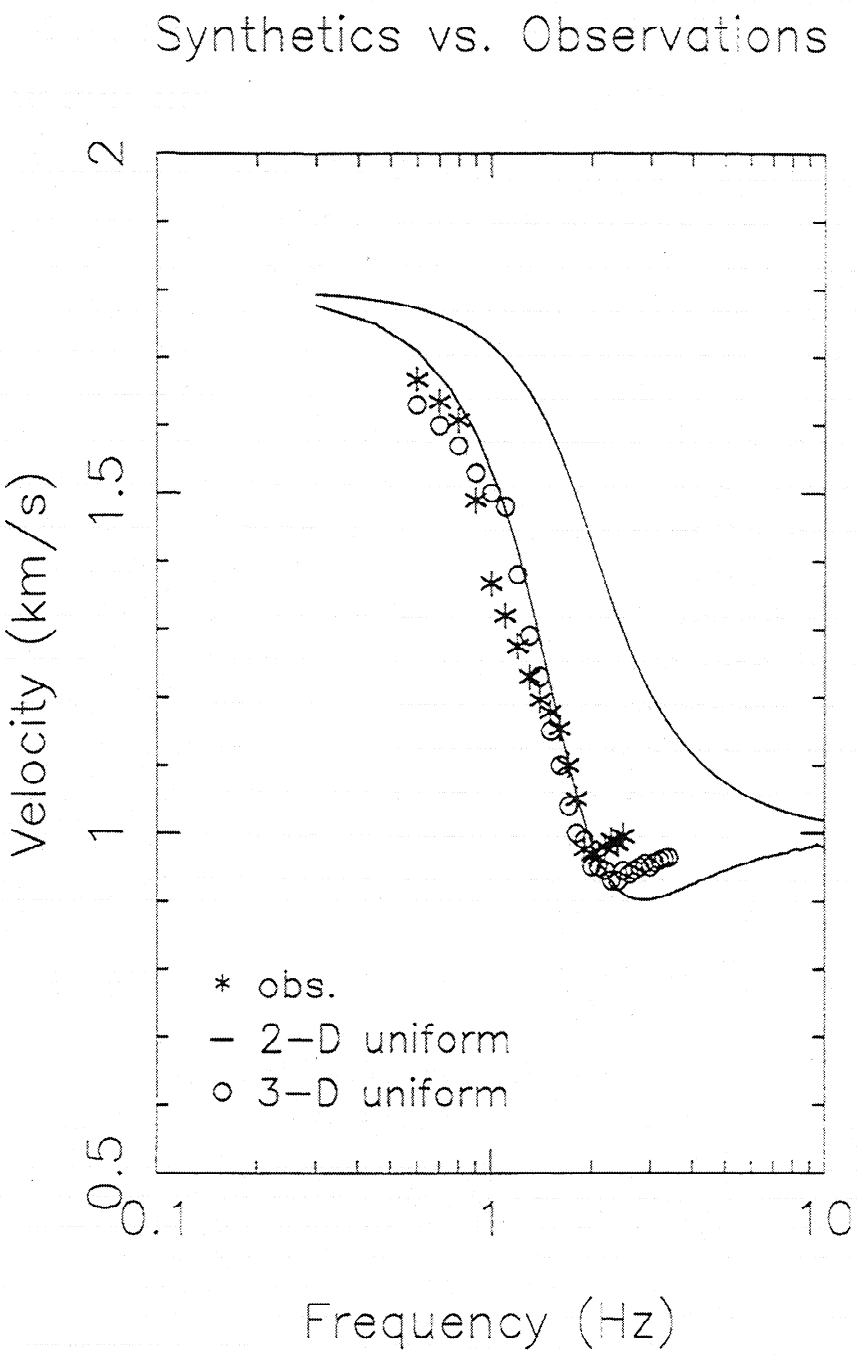

Figure 14. Group velocities derived from observations (stars) on line 2 for shot SP3, 3-D synthetics (circles), and 2-D synthetic dispersion curves (lines). Both 2-D and 3-D synthetics are computed using a uniform waveguide.

when we used model parameters shown in Table 2: the fault zone width is 250 m, shear velocity is 1.9 km/s and Q is 20 applied to the depth of ~1 km; the fault zone shear velocity increases to 1.9 km/s and Q increases to 30 below this depth.

However, the model parameters obtained from explosion-excited trapped waves are appropriate only for the shallow structure of the Johnson Valley fault because of the limit to the distance between the explosions and seismic arrays. Recently, we evaluated the depth-dependent fault zone structure using trapped waves from Landers aftershocks occurring at different depths between 1.8 and 8.2 km plus the results from near-surface explosion-excited trapped waves in a systematic model parameter-searching procedure using a 3-D finite difference computer code. Results reveal that the Landers fault zone is 250 m wide at the surface, tapering to 100-150 m at 8.2 km depth. The shear-velocity within the fault zone increases from 1.0 km/s to 2.5 km/s and Q increases from 20 to 60 in this depth range. The depth-variable structure of the Landers fault zone resulting from aftershock data are described in a separate paper.

In the present paper, we have described a delineation of the shallow Landers fault with high-resolution using explosion-excited trapped waves. Results from this study help us understand the developments of the fault trace at the surface but are also necessary for stripping off shallow effects to resolve internal fault zone structure deeper in the seismogenic zone.

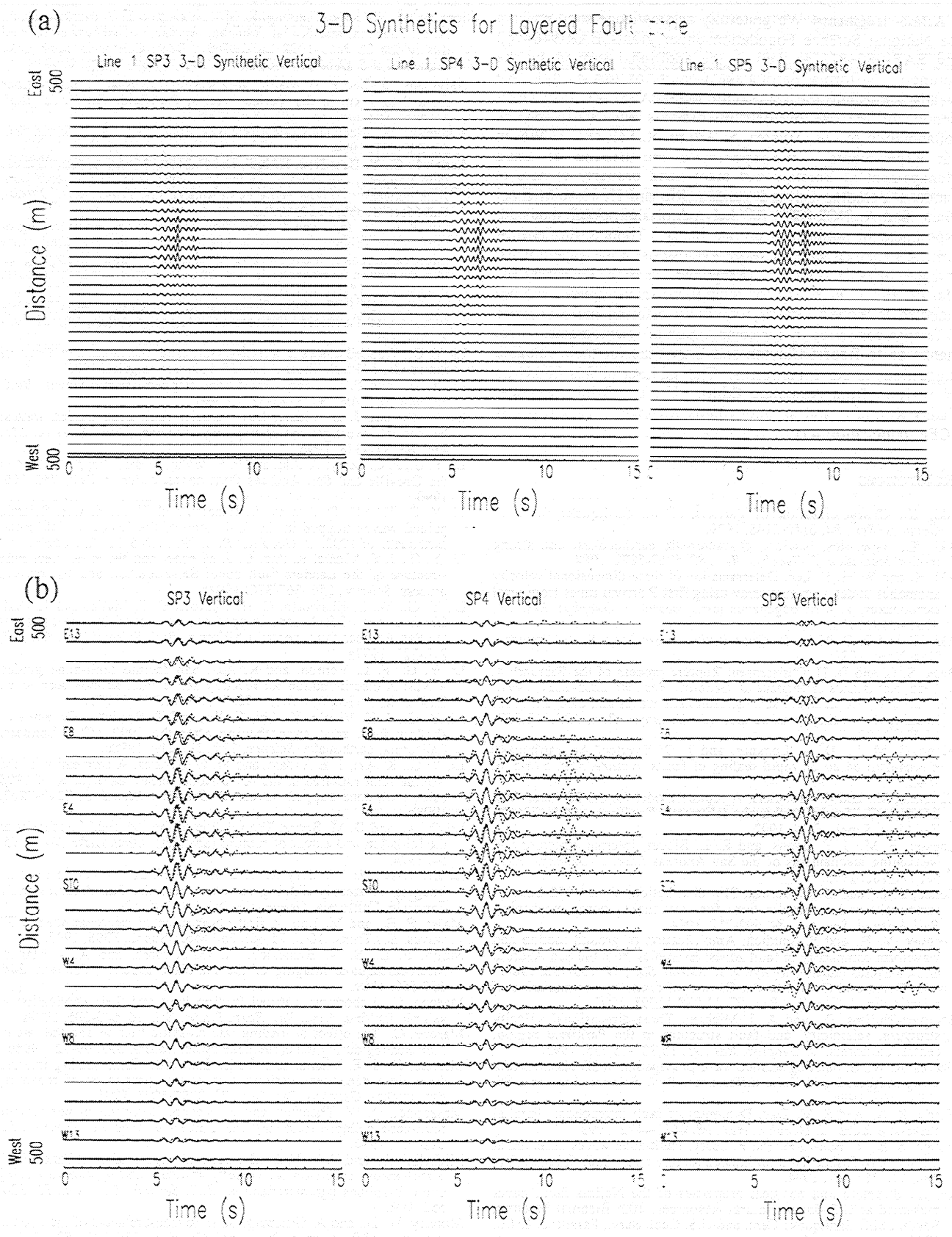

Figure 15. (a) Vertical component 3-D synthetic seismograms in cross-fault files on line 1 for shots SP3, SP4, and SP5 using a two-layer model with the model parameter given in Table 2. The station spacing is 25 m. Seismograms are plotted using a fixed amplitude scale for all traces. (b) A comparison of 3-D synthetics (dotted lines) with observations (solid lines) in cross-fault files on line 1 for shots SP3, SP4, and SP5. Both synthetic and recorded seismograms have been filtered in a frequency range of 0.7-1.8 Hz. Station spacings for synthetics are the same as in the field.

Acknowledgments. We gratefully acknowledge support from the National Science Foundation under grants EAR-9404762 and EAR-9804811 as well as the additional support by the Southern California Earthquake Center for this study. We greatly appreciate the support of IRIS-PASSCAL Instrument Center for the use of their instruments and thank for the collaboration of M. Alvarez, S. Arturo, R. Sell and A. Wei in our experiments. We appreciate the Bureau of Land Management at Barstow and many land property owners at Landers, including Edward Landau, Richard Hawley, Michael Clark, and Ann Cloutier, for their permission to carry out the experiment in public and private lands. Thomas Burdette of the USGS helped us to detonate explosions in the experiments, and we thank D. Adams, D. Bowman, G. Ely, K. Favret, A. Martin, and J. Wedberg for their work in the field. We are indebted to Robert Graves for kindly offering the 3-D finite difference code used in our computation of seismograms. Also, thanks go to Robert Clayton and Gary Fuis for their valuable suggestions to our experiments. The manuscript was improved by reviews from Associate Editor Uri ten Brink, reviewer Valeri Korneev, and an anonymous reviewer. This paper is SCEC publication 471.

References

Aki, K., Characterization of barriers on an earthquake fault, *J. Geophys. Res.*, 84, 6140-6148, 1979.

Aki, K., Asperities, barriers, characteristic earthquakes, and strong motion prediction, *J. Geophys. Res.*, *89*, 5867-5872, 1984.

Aki, K. and W. H. K. Lee, Determination of three-dimensional velocity anomalies under a seismic array using first P arrival times from local earthquakes, 1, A homogeneous initial model, *J. Geophys. Res.*, *81*, 4381-4399, 1976.

Aki, K., and P. C. Richards, *Quantitative Seismology*, W. H. Freeman, New York, 1980.

Beck, S. L. and D. H. Christensen, Rupture process of the February 4, 1965, Rat Islands earthquake, *J. Geophys. Res.*, *96*, 2205-2221, 1991.

Ben-Zion, Y., Properties of seismic fault zone waves and their utility for imaging low-velocity structure, *J. Geophys. Res.*, *103*, 12,567-12,585, 1998.

Blanpied, M. L., D. A. Lockner, and J. D. Byerlee, An earthquake mechanism based on rapid sealing of faults, *Nature*, *359*, 574-576, 1992.

Campillo, M., and R. Archuleta, A rupture model for the 28 June, 1992 Landers, California, earthquake (abstract), *Eos Trans. AGU*, *73*(43), Fall Meet. Suppl., F374, 1992.

Chester, F. M., J. P. Evans, and R. L. Biegel, Internal structure and weakening mechanisms of the San Andreas fault, *J. Geophys. Res.*, *98*, 771-786, 1993.

Cohee, B. P., and G. C. Beroza, Slip distribution of the 1992 Landers earthquake and its implications for earthquake source mechanics, *Bull. Seismol. Soc. Am.*, *84*, 692-712, 1994.

Cormier, V. F., and P. Spudich, Amplification of ground motion and waveform complexity in fault zones: Examples from the San Andreas and Calaveras faults, *Geophys. J. R. Astron. Soc.*, *79*, 135-152, 1984.

Cowie, P. A., and C. H. Scholz, Growth of faults by accumulation of seismic slip, *J. Geophys. Res.*, *97*, 11,085-11095, 1992.

Eberhart-Phillips, D., and A. J. Michael, Three-dimensional velocity structure, seismicity, and fault structure in the Parkfield region, central California, *J. Geophys. Res.*, *98*, 15,737-15,758, 1993.

Graves, R. W., Simulating seismic wave propagation in 3D elastic media using staggered-grid finite differences, *Bull. Seismol. Soc. Am.*, *86*, 1091-1106, 1996.

Harris, R. A., and S. M. Day, Dynamics of fault interaction: Parallel strike-slip faults, *J. Geophys. Res.*, *98*, 4461-4472, 1993.

Hough, S. E., Y. Ben-Zion, and P. Leary, Fault-zone waves observed at the southern Joshua Tree earthquake rupture zone, *Bull. Seismol. Soc. Am.*, *84*, 761-767, 1994.

Ito, H., Structure and physical properties of the Nojima fault, paper presented at U.S.-Japan Natural Resources, 10th Biennial Meeting, South. Calif. Earthquake Cent. and U.S. Geol. Surv., Pasadena, Calif., 1996.

Ito, H., and Y. Kuwahara, Trapped waves along the Nojima fault from the aftershock of Kobe earthquake, 1995 (abstract), *Eos Trans. AGU*, *76*(46), Fall Meet. Suppl., F377, 1995.

Johnson, A. M., R. W. Fleming, and K. M. Cruikshank, Shear zones formed along long, straight traces of fault zones during the 28 June 1992 Landers, California, earthquake, *Bull. Seismol. Soc. Am.*, *84*, 499-510, 1994.

Johnson, A. M., R. W. Fleming, K. M. Cruikshank, S. Y. Martosudarmo, N. A. Johnson, and K. M. Johnson, Analecta of structures formed during the 28 June 1992 Landers-Big Bear, California earthquake sequence, *U.S. Geol. Surv. Open File Rep.*, *97-94*, 59 pp., 1997.

Jongmans, D., and P. E. Malin, Microearthquake S-wave observations from 0 to 1 km in the Varian Well at Parkfield, California, *Bull. Seismol. Soc. Am.*, *85*, 1805-1820, 1995.

Kanamori, H., Mechanics of earthquakes, *Annu. Rev. Earth Planet. Sci.*, 22, 207-237, 1994.

Leary, P. C., Y. Ben-Zion, H. Igel, and P. Mora, Modeling San Andreas fault trapped waves with a 2D analytic expression for a layered fault zone between two quarterspaces (abstract), *Eos Trans. AGU*, *72*(44), Fall Meet. Suppl., F307, 1991a.

Leary, P. C., H. Igel, and Y. Ben-Zion, Observation and modeling of fault zone seismic trapped waves in aid of precise precursory microearthquake location and evaluation, paper presented at Conference on Earthquake Prediction: State-of-the Art, Strasbourg, France, Oct. 15-18, 1991b.

Lees, J. M., and P. E. Malin, Tomographic images of *P* wave velocity variation at Parkfield, California, *J. Geophys. Res.*, *95*, 21,793-21,804, 1990.

Li, Y. G., Trapped modes in a transversely isotropic fault-zone, Univ. of South. Calif., Ph.D. Thesis, pp. 168-189, Los Angeles, 1988.

Li, Y. G., and P. C. Leary, Fault zone trapped seismic waves, *Bull. Seismol. Soc. Am.*, *80*, 1245-1271, 1990.

Li, Y. G., and J. E. Vidale, Low-velocity fault zone guided waves: Numerical investigations of trapping efficiency, *Bull. Seismol. Soc. Am.*, *86*, 371-378, 1996.

Li, Y. G., P. C. Leary, K. Aki, and P. E. Malin, Seismic trapped modes in the Oroville and San Andreas fault zones, *Science*, *249*, 763-766, 1990.

Li, Y. G., K. Aki, D. Adams, A. Hasemi, and W. H. K. Lee, Seismic guided waves trapped in the fault zone of the Landers, California, earthquake of 1992, *J. Geophys. Res.*, *99*, 11,705-11,722, 1994a.

Li, Y. G., J. E. Vidale, K. Aki, C. J. Marone, and W. H. K. Lee, Fine structure of the Landers fault zone: Segmentation and the rupture process, *Science*, *256*, 367-370, 1994b.

Li, Y. G., W. L. Ellsworth, C. H. Thurber, P. E. Malin, and K. Aki, Observations of fault-zone trapped waves excited by explosions at the San Andreas fault, central California, *Bull. Seismol. Soc. Am.*, *87*, 210-221, 1997a.

Li, Y. G., F. L. Vernon, and K. Aki, San Jacinto fault-zone guided waves: A discrimination for recently active fault strands near Anza, California, *J. Geophys. Res.*, *102*, 11,689-11,701, 1997b.

Li, Y. G., J. E. Vidale, K. Aki, F. Xu, and T. Burdette, Evidence of shallow fault zone strengthening after the 1992 *M*7.5 Landers, California, earthquake, *Science*, *279*, 217-219, 1998a.

Li, Y. G., K. Aki, J. E. Vidale, and M. G. Alvarez, A delineation of the Nojima fault ruptured in the *M*7.2 Kobe, Japan, earthquake of 1995 using fault zone trapped waves, *J. Geophys. Res.*, *103*, 7247-7263, 1998b.

Lindh, A., and D. M. Boore, The relation of the Parkfield foreshocks to the initiation and extent of rupture (abstract), *Earthquake Notes*, *45*, 54, 1974.

Louie, J. N., R. W. Clayton, and R. J. LeBras, Three-dimensional imaging of steeply dipping structure near the San Andreas fault, Parkfield, California, *Geophysics*, *53*, 176-185, 1988.

Malin, P. E., and M. Lou, A first observation of microearthquake FR waves, *Eos Trans. AGU*, *76*(46), Fall Meet. Suppl., F398, 1995.

Malin, P. E., S. N. Blakeslee, M. G. Alvarez, and A. J. Martin, Microearthquake imaging of the Parkfield asperity, *Science*, *244*, 557-559, 1989.

Marone, C., Laboratory-derived friction laws and their application to seismic faulting, *Annu. Rev. Earth Planet. Sci.*, *26*, 643-696, 1998a.

Marone, C., The effect of loading rate on static friction and the rate of fault healing during the earthquake cycle, *Nature*, *391*, 69-72, 1998b.

Marone, C., J. E. Vidale, and W. L. Ellsworth, Fault healing inferred from time dependent variations in source properties of repeating earthquakes, *Geophys. Res. Lett.*, *22*, 3095-3098, 1995.

Massonnet, D., W. Thatcher, and H. Vadon, Detection of postseismic fault-zone collapse following the Landers earthquake, *Nature*, *382*, 612-616, 1996.

Michelini, A., and T. V. McEvilly, Seismological studies at Parkfield, I, Simultaneous inversion for velocity structure and hypocenters using cubic B-splines parameterization, *Bull. Seismol. Soc. Am.*, *81*, 524-552, 1991.

Mooney, W. D., and A. Ginzburg, Seismic measurements of the internal properties of fault zones, *Pure Appl. Geophys.*, *124*, 141-157, 1986.

Nicholson, C., and J. M. Lees, Travel-time tomography in the northern Coachella Valley using aftershocks of the 1986 ML 5.9 North Palm Springs earthquake, *Geophys. Res. Lett.*, *19*, 1-4, 1992.

Nishigami, K., Y. Fujiwara, and Y. Shimada, Fault-zone trapped waves observed at the Nojima fault for aftershocks accompanying the 1995 Kobe earthquake (abstract), *Eos Trans. AGU*, *76*(46), Fall Meet. Suppl., F378, 1995.

Nur, A., Dilatancy, pore fluid, and premonitory variations of ts/tp travel times, *Bull. Seismol. Soc. Am.*, *62*, 1217-1222, 1972.

Papageorgiou, A. S., and K. Aki, A specific barrier model for the quantitative description of inhomogeneous faulting and the prediction of strong motion, I, Description of the model, *Bull. Seismol. Soc. Am.*, *73*, 693-722, 1983.

Rice, J. R., The mechanics of earthquake rupture, in *Physics of the Earth's Interior*, edited by A. M. Dziewonski and E. Boschi, pp. 555-649, North-Holland, Amsterdam, 1980.

Scholz, C. H., *The Mechanics of Earthquakes and Faulting*, Cambridge Univ. Press, New York, 1990.

Scott, J. S., T. G. Masters, and F. L. Vernon, Three-dimensional velocity structure of the San Jacinto fault zone near Anza, California, I, P-waves, *Geophys. J. Int.*, *119*, 611-626, 1994.

Sibson, R. H., Fault rocks and fault mechanisms, *J. Geol. Soc. London*, *133*, 191-213, 1977.

Sieh, K., et al., Near-field investigations of the Landers earthquake sequence, April to July 1992, *Science*, *260*, 171-176, 1993.

Thurber, C. H., Earthquake locations and three-dimensional crustal structure in the Coyote Lake area, central California, *J. Geophys. Res.*, *88*, 8226-8236, 1983.

Thurber, C. H., S. Roecker, W. Ellsworth, Y. Chen, W. Lutter, and R. Sessions, Two-dimensional seismic image of the San Andreas fault in the northern Gabilan Range, central California: Evidence for fluids in the fault zone, *Geophys. Res. Lett.*, *24*, 1591-1594, 1997.

Vidale, J. E., W. L. Ellsworth, A. Cole, and C. Marone, Rupture variation with recurrence interval in eighteen cycles of a small earthquake, *Nature*, 368, 624-626, 1994.

Wald, D. J., and T. H. Heaton, Spatial and temporal distribution of slip for the 1992 Landers, California, earthquake, *Bull. Seismol. Soc. Am.*, *84*, 668-691, 1994.

K. Aki and Y.-G. Li, Department of Earth Sciences, University, of Southern California, Los Angeles, CA 90089-0740. (ygli@terra.usc.edu; kaki@usc.edu)

J. E. Vidale and F. Xu, Deparmtnent of Earth and Space Sciences, University of California, Los Angeles, CA 90095-1567. (vidale@moho.ess.ucla.edu; fxu@ess.ucla.edu)

(Received August 5, 1998; revised April 14, 1999; accepted June 2, 1999)